The Frequency-Domain Moment-Tensor Inversion: Retrieving the Complete Source Moment-Tensor Spectra and Time Histories

Xiaoning Yang, Brian W. Stump and Mason D. Macphail

1 Introduction

When the wavelength of a seismic signal of interest is much longer than the dimension of the internal seismic source that generates the signal, whether it is an earthquake, an underground explosion or an underground mine collapse, the seismic source may be represented by a symmetric second-order moment tensor. The observed seismic signal is then the convolution of the source moment tensor with the earth's impulse response, or the Green's function between the source and the receiver, which records the signal. This relationship is universally used to retrieve the source moment tensor from observed seismic data for seismic-source characterizations. Assuming a step source time function, research organizations use seismic body waves, surface waves and the earth's free oscillation to routinely calculate moment tensors of global earthquakes (e.g., Ekström et al. 2012; Pondrelli et al. 2011; Tsuruoka et al. 2009). For detailed source analysis, seismologists also attempt to recover source time functions that are not a step function using either time-domain methods (e.g., Sipkin 1982; Šílený et al. 1992) or a frequency-domain approach (e.g., Stump and Johnson 1977).

Here we describe the frequency-domain moment-tensor inversion method of Stump and Johnson (1977) including its mathematical formulation, the inversion method and error assessments. We also provide some examples to illustrate the application of the method.

Los Alamos National Laboratory unlimited release number: LA-UR-17-22976.

X. Yang (✉)
Los Alamos National Laboratory, Los Alamos, NM 87545, USA
e-mail: xyang@lanl.gov

B. W. Stump · M. D. Macphail
Southern Methodist University, Dallas, TX 75275, USA

S. D'Amico (ed.), *Moment Tensor Solutions*, Springer Natural Hazards,
https://doi.org/10.1007/978-3-319-77359-9_3

2 Theory

The basic relationship between the ground displacement and the seismic source excitation is the representation theorem. The theorem states that ground displacement u_n ($n=1, 2, 3$) at location $\mathbf{x}$ and time t due to the equivalent body-force density f_i, which includes contributions from the body force, the initial condition and the boundary condition, is

$$u_n(\mathbf{x}, t) = \int_{-\infty}^{\infty} \left[\int\int\int_V G_{ni}(\mathbf{x}, t-\tau; \boldsymbol{\xi}, 0) f_i(\boldsymbol{\xi}, \tau) dV(\boldsymbol{\xi}) \right] d\tau, \tag{1}$$

where G_{ni} is the Green's function and the volume V contains all nonzero f_i (Aki and Richards 2002). Einstein summation is assumed for all equations in this article. By expanding the Green's function in a Taylor series about the coordinate origin, we have

$$G_{ni}(\mathbf{x}, t-\tau; \boldsymbol{\xi}, \mathbf{0}) = \sum_{m=0}^{\infty} \frac{1}{m!} \xi_{j_1} \ldots \xi_{j_m} G_{ni, j_1 \ldots j_m}(\mathbf{x}, t-\tau; \mathbf{0}, 0), \tag{2}$$

where $G_{ni, j_1 \cdots j_m}$ is the mth spatial derivative of the Green's function. If we define the force moment tensor of order $m+1$ as

$$M_{i j_1 \ldots j_m}(\mathbf{0}, \tau) = \int\int\int_V \xi_{j_1} \ldots \xi_{j_m} f_i(\boldsymbol{\xi}, \tau) dV(\boldsymbol{\xi}), \tag{3}$$

Equation (1) becomes

$$\begin{aligned} u_n(\mathbf{x}, t) &= \int_{-\infty}^{\infty} \left[\sum_{m=0}^{\infty} \frac{1}{m!} G_{ni, j_1 \ldots j_m}(\mathbf{x}, t-\tau; \mathbf{0}, 0) M_{i j_1 \ldots j_m}(\mathbf{0}, \tau) \right] d\tau \\ &= \sum_{m=0}^{\infty} \frac{1}{m!} \int_{-\infty}^{\infty} G_{ni, j_1 \ldots j_m}(\mathbf{x}, t-\tau; \mathbf{0}, 0) M_{i j_1 \ldots j_m}(\mathbf{0}, \tau), \\ &= \sum_{m=0}^{\infty} \frac{1}{m!} \int_{-\infty}^{\infty} G_{ni, j_1 \ldots j_m}(\mathbf{x}, t; \mathbf{0}, 0) * M_{i j_1 \ldots j_m}(\mathbf{0}, t) \end{aligned} \tag{4}$$

where * denotes temporal convolution (Stump and Johnson 1977; Julian et al. 1998).

If we assume that the linear momentum of the body-force system is conserved during the source process, which is usually true for sources internal to the earth such as earthquakes and underground explosions, then from Eq. (3),

$$M_i(\mathbf{0}, \tau) = \int \int \int_V f_i(\boldsymbol{\xi}, \tau)\, dV(\boldsymbol{\xi}) = 0.$$

In addition, if the volume of the body-force system is much smaller than the wavelength of the seismic wave that the source generates, terms with orders higher than $m = 1$ in the Green's function expansion (Eq. 2) can be neglected (Stump and Johnson 1977). As a result, Eq. (4) is reduced to

$$u_n(\mathbf{x}, t) = G_{ni,j}(\mathbf{x}, t; \mathbf{0}, 0) * M_{ij}(\mathbf{0}, t). \tag{5}$$

For internal seismic sources, the angular momentum of the source system is usually conserved. It can be shown that for such sources, the source moment tensor M_{ij} is symmetric with six independent components (Aki and Richards 2002). If we Fourier transform Eq. (5) into the frequency domain, convolution becomes multiplication and we obtain

$$u_n(\mathbf{x}, f) = G_{ni,j}(\mathbf{x}, f; \mathbf{0}, 0) M_{ij}(\mathbf{0}, f). \tag{6}$$

Equation (6) is the basic equation that we use to describe the frequency-domain moment-tensor-inversion method.

3 Methodology

To invert Eq. (6) for the source moment tensor M_{ij}, we use ground-motion data recorded by multiple receivers at different azimuths and distances from the source. In order to facilitate the inversion, we first partition ground-motion data into radial, transverse and vertical components with the projection of the direction from the source to the receiver on a horizontal plane as the radial direction. We then represent the ground motion as a function of the source moment tensor defined in the source coordinate system. We describe the procedure in detail below.

Without loss of generality, we abbreviate Eq. (6) to

$$u_n = G_{ni,j} M_{ij}. \quad (n = 1, 2, 3) \tag{7}$$

We assume that Eq. (7) is defined in a coordinate system with its origin at the source, and with x_1-axis positive to the north, x_2-axis positive to the east and x_3-axis positive down. We call this system the source coordinate system. Considering a receiver that is located at θ-degree azimuth from the source, we establish another coordinate system that has the same origin as the source coordinate system, but with axes in radial ($x_{1'}$), transverse ($x_{2'}$) and vertical ($x_{3'}$) directions. For this coordinate system, the horizontal direction θ degrees from the north is radial positive, the horizontal direction 90° clockwise from radial positive is transverse positive and

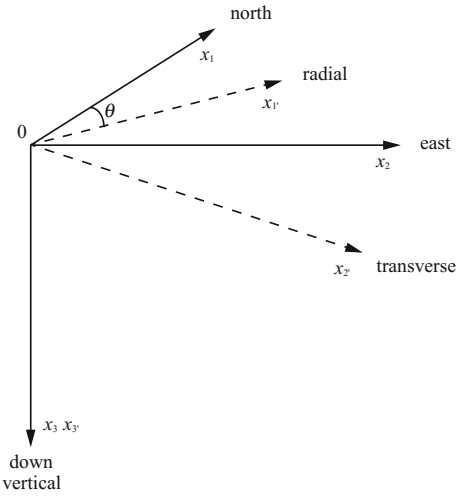

Fig. 1 Definition of and relationship between source and receiver coordinate systems

down is vertical positive (Fig. 1). We refer to this system as the receiver coordinate system.

In the receiver coordinate system, Eq. (7) becomes

$$u_{n'} = G_{n'i',j'} M_{i'j'}. \tag{8}$$

According to the transformation law for a second-order tensor,

$$M_{i'j'} = \alpha_{ii'} \alpha_{jj'} M_{ij}, \tag{9}$$

where α_{ij} are direction cosines from the transformation matrix between the source and the receiver coordinate systems:

$$\boldsymbol{\alpha} = \begin{bmatrix} \alpha_{11'} & \alpha_{12'} & \alpha_{13'} \\ \alpha_{21'} & \alpha_{22'} & \alpha_{23'} \\ \alpha_{31'} & \alpha_{32'} & \alpha_{33'} \end{bmatrix} = \begin{bmatrix} \cos\theta & -\sin\theta & 0 \\ \sin\theta & \cos\theta & 0 \\ 0 & 0 & 1 \end{bmatrix}. \tag{10}$$

Using Eq. (10) to expand Eq. (9), we have

$$\begin{aligned}
M_{1'1'} &= M_{11}\cos^2\theta + 2M_{12}\cos\theta\ \sin\theta + M_{22}\sin^2\theta \\
M_{1'2'} &= (M_{22} - M_{11})\sin\theta\ \cos\theta - M_{12}\left(\sin^2\theta - \cos^2\theta\right) \\
M_{1'3'} &= M_{13}\cos\theta + M_{23}\sin\theta \\
M_{2'2'} &= M_{11}\sin^2\theta - 2M_{12}\cos\theta\ \sin\theta + M_{22}\cos^2\theta \\
M_{2'3'} &= M_{23}\cos\theta - M_{13}\sin\theta \\
M_{3'3'} &= M_{33}
\end{aligned} \tag{11}$$

Substituting Eq. (11) into the expansion of Eq. (8) yields

$$\begin{aligned} u_{n'} = {} & M_{11}[\cos^2\theta G_{n'1',1'} + \sin^2\theta G_{n'2',2'} - \cos\theta\ \sin\theta(G_{n'1',2'} + G_{n'2',1'})] \\ & + M_{12}[2\cos\theta\ \sin\theta(G_{n'1',1'} - G_{n'2',2'}) + (\cos^2\theta - \sin^2\theta)(G_{n'1',2'} + G_{n'2',1'})] \\ & + M_{13}[\cos\theta(G_{n'1',3'} + G_{n'3',1'}) - \sin\theta(G_{n'2',3'} + G_{n'3',2'})] \\ & + M_{22}[\sin^2\theta G_{n'1',1'} + \cos^2\theta G_{n'2',2'} + \sin\theta\ \cos\theta(G_{n'1',2'} + G_{n'2',1'})] \\ & + M_{23}[\sin\theta(G_{n'1',3'} + G_{n'3',1'}) + \cos\theta(G_{n'2',3'} + G_{n'3',2'})] \\ & + M_{33}G_{n'3',3'} \end{aligned} , \tag{12}$$

which expresses the ground displacement in the receiver coordinate system in terms of the source moment tensor in the source coordinate system. If we denote $x_{1'}$ as r, $x_{2'}$ as t and $x_{3'}$ as z, we arrive at the equation that we use for the moment-tensor inversion:

$$\begin{aligned} u_r = {} & M_{11}[\cos^2\theta G_{rr,r} + \sin^2\theta G_{rt,t} - \cos\theta\ \sin\theta(G_{rr,t} + G_{rt,r})] \\ & + M_{12}[2\cos\theta\ \sin\theta(G_{rr,r} - G_{rt,t}) + (\cos^2\theta - \sin^2\theta)(G_{rr,t} + G_{rt,r})] \\ & + M_{13}[\cos\theta(G_{rr,z} + G_{rz,r}) - \sin\theta(G_{rt,z} + G_{rz,t})] \\ & + M_{22}[\sin^2\theta G_{rr,r} + \cos^2\theta G_{rt,t} + \sin\theta\ \cos\theta(G_{rr,t} + G_{rt,r})] \\ & + M_{23}[\sin\theta(G_{rr,z} + G_{rz,r}) + \cos\theta(G_{rt,z} + G_{rz,t})] \\ & + M_{33}G_{rz,z} \\ u_t = {} & M_{11}[\cos^2\theta G_{tr,r} + \sin^2\theta G_{tt,t} - \cos\theta\ \sin\theta(G_{tr,t} + G_{tt,r})] \\ & + M_{12}[2\cos\theta\ \sin\theta(G_{tr,r} - G_{tt,t}) + (\cos^2\theta - \sin^2\theta)(G_{tr,t} + G_{tt,r})] \\ & + M_{13}[\cos\theta(G_{tr,z} + G_{tz,r}) - \sin\theta(G_{tt,z} + G_{tz,t})] \\ & + M_{22}[\sin^2\theta G_{tr,r} + \cos^2\theta G_{tt,t} + \sin\theta\ \cos\theta(G_{tr,t} + G_{tt,r})] \\ & + M_{23}[\sin\theta(G_{tr,z} + G_{tz,r}) + \cos\theta(G_{tt,z} + G_{tz,t})] \\ & + M_{33}G_{tz,z} \\ u_z = {} & M_{11}[\cos^2\theta G_{zr,r} + \sin^2\theta G_{zt,t} - \cos\theta\ \sin\theta(G_{zr,t} + G_{zt,r})] \\ & + M_{12}[2\cos\theta\ \sin\theta(G_{zr,r} - G_{zt,t}) + (\cos^2\theta - \sin^2\theta)(G_{zr,t} + G_{zt,r})] \\ & + M_{13}[\cos\theta(G_{zr,z} + G_{zz,r}) - \sin\theta(G_{zt,z} + G_{zz,t})] \\ & + M_{22}[\sin^2\theta G_{zr,r} + \cos^2\theta G_{zt,t} + \sin\theta\ \cos\theta(G_{zr,t} + G_{zt,r})] \\ & + M_{23}[\sin\theta(G_{zr,z} + G_{zz,r}) + \cos\theta(G_{zt,z} + G_{zz,t})] \\ & + M_{33}G_{zz,z} \end{aligned} . \tag{13}$$

To use Eq. (13) in the moment-tensor inversion, we need to calculate 3-component Green's functions for the 6 moment-tensor components, which amounts to a total of 18 Green's functions. If the earth medium is horizontally homogeneous and isotropic, which we often assume, Eq. (13) can be further simplified. This is because for such an earth model, we have

$$\begin{aligned} G_{tr,r} = {} & G_{tt,t} = G_{tz,z} = G_{tr,z} + G_{tz,r} = G_{rr,t} + G_{rt,r} \\ = {} & G_{rt,z} + G_{rz,t} = G_{zr,t} + G_{zt,r} = G_{zt,z} + G_{zz,t} = 0. \end{aligned}$$

This conclusion can be proven by expanding Eq. (4.29) of Aki and Richards (2002) and realizing that when the source moment tensor and the ground motion are expressed in the same receiver coordinate system, for a horizontally homogeneous and isotropic earth model, the ray path between the source and the receiver is always in the r-z plane and the direction cosine γ_t is zero. With this observation, Eq. (13) becomes

$$\begin{aligned}
u_r &= M_{11}[\cos^2\theta G_{rr,r} + \sin^2\theta G_{rt,t}] \\
&\quad + M_{12}[2\cos\theta\ \sin\theta(G_{rr,r} - G_{rt,t})] \\
&\quad + M_{13}[\cos\theta(G_{rr,z} + G_{rz,r})] \\
&\quad + M_{22}[\sin^2\theta G_{rr,r} + \cos^2\theta G_{rt,t}] \\
&\quad + M_{23}[\sin\theta(G_{rr,z} + G_{rz,r})] \\
&\quad + M_{33}G_{rz,z} \\
u_t &= -M_{11}[\cos\theta\ \sin\theta(G_{tr,t} + G_{tt,r})] \\
&\quad + M_{12}[(\cos^2\theta - \sin^2\theta)(G_{tr,t} + G_{tt,r})] \\
&\quad - M_{13}[\sin\theta(G_{tt,z} + G_{tz,t})] \\
&\quad + M_{22}[\sin\theta\ \cos\theta(G_{tr,t} + G_{tt,r})] \\
&\quad + M_{23}[\cos\theta(G_{tt,z} + G_{tz,t})] \\
u_z &= M_{11}[\cos^2\theta G_{zr,r} + \sin^2\theta G_{zt,t}] \\
&\quad + M_{12}[2\cos\theta\ \sin\theta(G_{zr,r} - G_{zt,t})] \\
&\quad + M_{13}[\cos\theta(G_{zr,z} + G_{zz,r})] \\
&\quad + M_{22}[\sin^2\theta G_{zr,r} + \cos^2\theta G_{zt,t}] \\
&\quad + M_{23}[\sin\theta(G_{zr,z} + G_{zz,r})] \\
&\quad + M_{33}G_{zz,z}
\end{aligned} \qquad . \tag{14}$$

Next, we express Eq. (14) in terms of the 10 specific, sometimes called canonical, Green's functions. First, we define 4 types of sources in the source coordinate system. We require that the time dependence of all 4 sources is an impulse that starts at $t = 0$. Its Fourier transform is then 1. The first source is a left-lateral vertical strike-slip source with its fault in the $x_1 - x_3$ plane. Its moment tensor representation is

$$\mathbf{M}_{SS}(f) = \begin{bmatrix} 0 & 1 & 0 \\ 1 & 0 & 0 \\ 0 & 0 & 0 \end{bmatrix}. \tag{15a}$$

The second source is a vertical dip-slip source with the fault in the $x_1 - x_3$ plane and the slip direction of the footwall, the wall on the positive x_2 side of the fault, is vertically downwards. Its moment tensor is

$$\mathbf{M}_{DS}(f) = \begin{bmatrix} 0 & 0 & 0 \\ 0 & 0 & -1 \\ 0 & -1 & 0 \end{bmatrix}. \tag{15b}$$

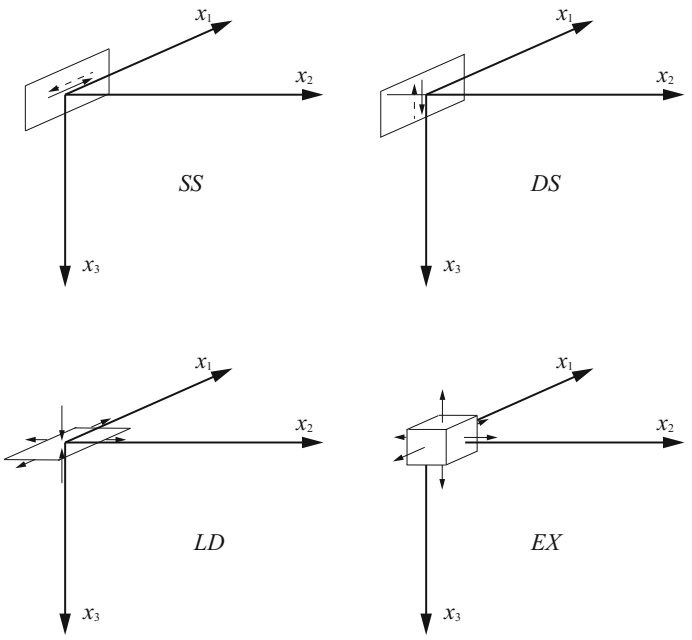

Fig. 2 Depiction of the four sources: strike slip (*SS*), dip slip (*DS*), CLVD (*LD*) and explosion (*EX*)

The third source is a compensated linear vector dipole (CLVD) with its vertical dipole twice as large as its horizontal dipoles. The moment tensor of this source is

$$\mathbf{M}_{LD}(f) = \begin{bmatrix} 0.5 & 0 & 0 \\ 0 & 0.5 & 0 \\ 0 & 0 & -1 \end{bmatrix}. \tag{15c}$$

The fourth source is an isotropic explosion with the moment tensor

$$\mathbf{M}_{EX}(f) = \begin{bmatrix} 1 & 0 & 0 \\ 0 & 1 & 0 \\ 0 & 0 & 1 \end{bmatrix}. \tag{15d}$$

The four sources are pictured in Fig. 2.

When we record seismic signals or compute synthetic seismograms from these four sources at specific azimuths, we obtain the 10 so-called canonical Green's functions. When the receiver is at an azimuth of 45° ($\pi/4$) from the strike-slip source, from Eqs. (14) and (15a), the radial- and vertical-component ground displacements are

$$\begin{aligned} SS_r &= u_r = M_{12}[2\cos\left(\frac{\pi}{4}\right)\sin\left(\frac{\pi}{4}\right)(G_{rr,r} - G_{rt,t})] = G_{rr,r} - G_{rt,t} \\ SS_z &= u_z = M_{12}[2\cos\left(\frac{\pi}{4}\right)\sin\left(\frac{\pi}{4}\right)(G_{zr,r} - G_{zt,t})] = G_{zr,r} - G_{zt,t} \end{aligned}. \tag{16a}$$

When the receiver is at an azimuth of 0° from the strike-slip source, the transverse component is

$$SS_t = u_t = M_{12}[(\cos^2(0) - \sin^2(0))(G_{tr,t} + G_{tt,r})] = G_{tr,t} + G_{tt,r}. \tag{16b}$$

For the dip-slip source, the radial and vertical components at an azimuth of 90° ($\pi/2$) are

$$\begin{aligned} DS_r &= u_r = M_{23}[\sin\left(\frac{\pi}{2}\right)(G_{rr,z} + G_{rz,r})] = -(G_{rr,z} + G_{rz,r}) \\ DS_z &= u_z = M_{23}[\sin\left(\frac{\pi}{2}\right)(G_{zr,z} + G_{zz,r})] = -(G_{zr,z} + G_{zz,r}) \end{aligned}. \tag{16c}$$

The transverse component from the dip-slip source at the azimuth of 0° is

$$DS_t = u_t = M_{23}[\cos(0)(G_{tt,z} + G_{tz,t})] = -(G_{tt,z} + G_{tz,t}). \tag{16d}$$

For CLVD and explosion sources, there is no transverse ground motion and the azimuth of the receiver can be arbitrary. For the CLVD source, we have

$$\begin{aligned} LD_r &= u_r = M_{11}[\cos^2\theta G_{rr,r} + \sin^2\theta G_{rt,t}] + M_{22}[\sin^2\theta G_{rr,r} + \cos^2\theta G_{rt,t}] + M_{33}G_{rz,z} \\ &= \frac{1}{2}(G_{rr,r} + G_{rt,t}) - G_{rz,z} \\ LD_z &= u_z = M_{11}[\cos^2\theta G_{zr,r} + \sin^2\theta G_{zt,t}] + M_{22}[\sin^2\theta G_{zr,r} + \cos^2\theta G_{zt,t}] + M_{33}G_{zz,z} \\ &= \frac{1}{2}(G_{zr,r} + G_{zt,t}) - G_{zz,z} \end{aligned}. \tag{16e}$$

For the explosion source, we have

$$\begin{aligned} EX_r &= u_r = M_{11}[\cos^2\theta G_{rr,r} + \sin^2\theta G_{rt,t}] + M_{22}[\sin^2\theta G_{rr,r} + \cos^2\theta G_{rt,t}] + M_{33}G_{rz,z} \\ &= G_{rr,r} + G_{rt,t} + G_{rz,z} \\ EX_z &= u_z = M_{11}[\cos^2\theta G_{zr,r} + \sin^2\theta G_{zt,t}] + M_{22}[\sin^2\theta G_{zr,r} + \cos^2\theta G_{zt,t}] + M_{33}G_{zz,z} \\ &= G_{zr,r} + G_{zt,t} + G_{zz,z} \end{aligned}. \tag{16f}$$

When we substitute Eq. (16a–16f) into Eq. (14), we obtain

$$
\begin{aligned}
u_r = & M_{11}\left[\frac{SS_r}{2}\cos 2\theta + \frac{EX_r + LD_r}{3}\right] \\
& + M_{12}[SS_r \sin 2\theta] \\
& - M_{13}[DS_r \cos\theta] \\
& - M_{22}\left[\frac{SS_r}{2}\cos 2\theta - \frac{EX_r + LD_r}{3}\right] \\
& - M_{23}[DS_r \sin\theta] \\
& - M_{33}\left[\frac{2}{3}\left(LD_r - \frac{EX_r}{2}\right)\right] \\
u_t = & -M_{11}\left[\frac{SS_t}{2}\sin 2\theta\right] \\
& + M_{12}[SS_t \cos 2\theta] \\
& + M_{13}[DS_t \sin\theta] \\
& + M_{22}\left[SS_t \frac{\sin 2\theta}{2}\right] \\
& - M_{23}[DS_t \cos\theta] \\
u_z = & M_{11}\left[\frac{SS_z}{2}\cos 2\theta + \frac{EX_z + LD_z}{3}\right] \\
& + M_{12}\left[SS_z \sin 2\theta\right] \\
& - M_{13}\left[DS_z \cos\theta\right] \\
& - M_{22}\left[\frac{SS_z}{2}\cos 2\theta - \frac{EX_z + LD_z}{3}\right] \\
& - M_{23}\left[DS_z \sin\theta\right] \\
& - M_{33}\left[\frac{2}{3}\left(LD_z - \frac{EX_z}{2}\right)\right]
\end{aligned}
\qquad . \tag{17}
$$

Equations (13) and (17) are the basic equations that are used to invert for the frequency-domain source moment tensor, or the moment-tensor spectra. With observations at multiple receivers, these equations can be expressed in the matrix form as

$$\mathbf{d} = \mathbf{G}\mathbf{m}, \tag{18}$$

where $\mathbf{d}$ contains Fourier-transformed ground motion, $\mathbf{G}$ contains frequency-domain Green's functions and $\mathbf{m}$ are frequency-domain moment-tensor components. With digital data, all spectra in Eq. (18) are for discrete frequencies.

Equation (18) can be solved for $\mathbf{m}$ at each frequency with standard least-squares inversion methods such as the singular-value-decomposition method (SVD) (e.g., Menke 1989), in which $\mathbf{G}$ is decomposed as

$$\mathbf{G} = \mathbf{U}\boldsymbol{\Lambda}\mathbf{V}^{\mathbf{H}},$$

where $\mathbf{U}$ is composed of eigenvectors of $\mathbf{G}\mathbf{G}^{\mathrm{H}}$ and $\mathbf{V}$ is composed of eigenvectors of $\mathbf{G}^{\mathrm{H}}\mathbf{G}$. Superscript $^{\mathrm{H}}$ denotes conjugate transpose. Diagonal matrix $\boldsymbol{\Lambda}$ contains

nonzero square roots of corresponding eigenvalues, called singular values. With the SVD method, the source moment tensor is estimated as

$$\mathbf{m}^{\mathbf{est}} = \mathbf{V}\boldsymbol{\Lambda}^{-1}\mathbf{U}^{\mathbf{H}}\mathbf{d}. \tag{19}$$

The complete source moment-tensor spectra are obtained by combining inversion results at individual frequencies. Time histories of the moment tensor are obtained by the inverse Fourier transform of the moment-tensor spectra.

For statistically independent ground-motion data with a uniform variance σ_d^2, the covariance of the estimated moment tensor is (Menke 1989)

$$\mathrm{cov}(\mathbf{m}^{\mathrm{est}}) = \sigma_d^2\mathbf{V}\boldsymbol{\Lambda}^{-2}\mathbf{V}^{\mathrm{H}}. \tag{20}$$

Equation (20) shows that the covariance and the variance of the estimated moment tensor depend on the singular-value matrix. Small singular values result in large moment-tensor variances.

The time history of a seismic source, whether it is an earthquake or an explosion, often has a static offset as time approaches infinity. The Fourier transform of this component approaches infinity as the frequency goes to zero. This low-frequency behavior makes the frequency-domain inversion results using ground displacements unstable. To stabilize the inversion at low frequencies, we usually use ground velocity, instead of ground displacement, in the moment-tensor inversion. As a result, the time derivative of the moment-tensor spectra, or the moment-rate-tensor spectra, is retrieved.

4 Examples

Because the purpose of using the frequency-domain moment-tensor-inversion technique is to retrieve the complete source moment-tensor spectra including its high-frequency component, this method is often employed to characterize small sources where the point-source approximation is more appropriate for high-frequency data. These sources include small earthquakes, e.g., induced seismicity, and man-made sources, such as underground explosions or mine collapses. In this section, we first give two examples demonstrating the technique in characterizing an underground chemical explosion and a unique underground-mine collapse. The final example illustrates the importance of accurate velocity models to inversion results.

4.1 An Underground Chemical Explosion

The first example is the moment-tensor inversion using near-source seismograms from an underground chemical explosion (Yang and Bonner 2009). The explosion

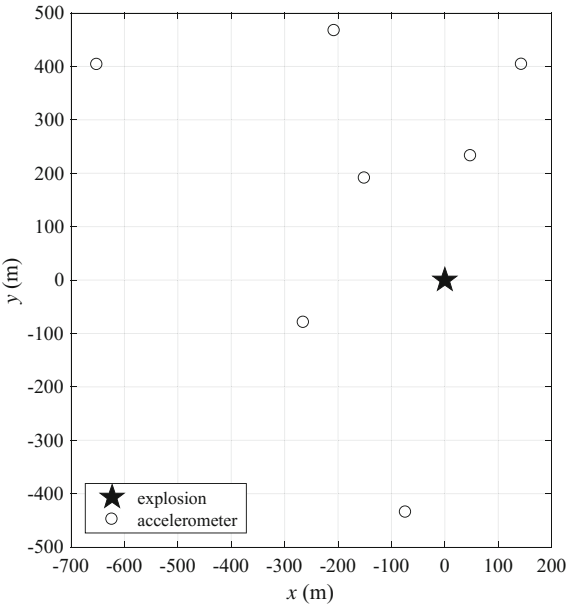

Fig. 3 Locations of the explosion source and accelerometers

source was constructed by drilling 5 holes in a cross pattern to a depth of 40 m, filling the holes with 10 m of explosives, and stemming the holes to the surface. The total weight of the explosive is 5484 kg. The arm length of the cross drill pattern is about 3.5 m. Explosives in the 5 holes were detonated simultaneously resulting in an effective single, contained explosion source. Seismic signals from this explosion were recorded by an accelerometer array around the source. Figure 3 plots the locations of the explosion and accelerometers. The source-receiver distances are from 201 to 668 m. The accelerometers cover about half of the complete 360° azimuths. An optimal azimuthal coverage would span 360° for a complete sampling of the source radiation pattern. Considering the fact that the radiation pattern from an explosion source should be relatively uniform and the fact that three-component waveforms are utilized, this azimuthal coverage should be sufficient. Deployment of receivers at different distances is also desired for improved sampling of the source focal sphere.

Figure 4 displays the ground-velocity seismograms determined by integrating ground accelerations recorded at the receivers shown in Fig. 3. These are typical of seismic signals we see from explosive sources at close distances. The raw signals are generally short (<1 s). The main signal is the *P*-wave. If we low-pass filter the signals, short-distance, fundamental-mode Rayleigh wave (R_g) becomes significant. Even though explosive sources are supposed to generate mainly compressional waves, we usually see appreciable shear waves on the transverse component due to the potential asymmetry of the sources and/or media heterogeneity.

To invert these ground motions for the source moment tensor, we need to calculate Green's functions between the source and receivers. This in turn requires a proper

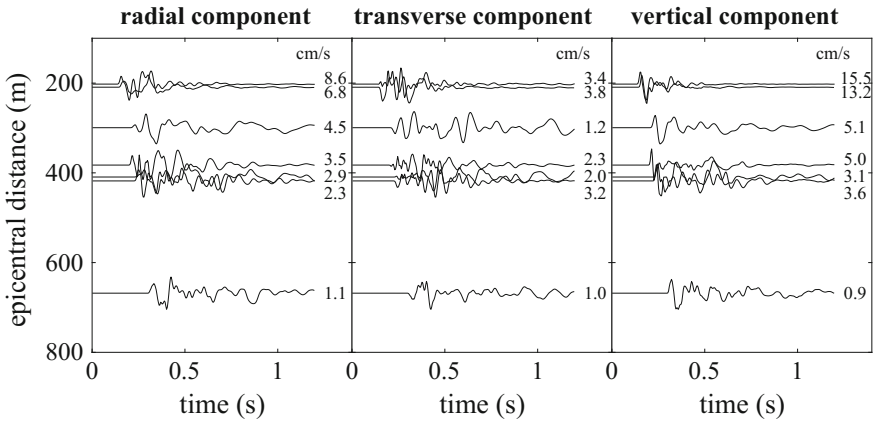

Fig. 4 Ground velocities from the explosion. Amplitudes are normalized. Maximum absolute amplitudes are marked to the right of the traces

earth model with *P*-wave velocity, *S*-wave velocity, density, *P*-wave quality factor Q_p and shear-wave quality factor Q_s. In many cases, because source signals are recorded at close distances (e.g., <2 km), the medium heterogeneity is not severe and a laterally homogeneous, one-dimensional (1D) earth model can be used. This assumption is good for this experiment where the explosion was detonated in sedimentary rocks with velocity changes mainly in the vertical direction. Generally, different parameters of the earth model are derived from different data types. In this example, *P*-wave velocity structure of the earth model was developed using *P*-wave arrival times from a refraction survey and from seismometers installed around the test site (Leidig et al. 2005). *S*-wave velocities were derived from surface-wave analysis, and density data were from laboratory sample tests. Shear-wave quality factor was from analysis of surface-wave amplitudes, whereas that of *P*-wave was based on a theoretical relationship between Q_s and Q_p (Müller 1985).

For 1D earth models, a variety of computation methods can be used to calculate synthetic seismograms, or Green's functions. In this example, we use a method called the reflectivity method (Müller 1985) for the calculation. The method is a slowness-integration method that generates complete seismograms including both near-field and far-field terms. Other than an accurate earth model, the key aspect of getting proper Green's functions using the method is to select appropriate input parameters, such as slowness-integration interval, slowness sampling and length of the time trace, for the problem at hand so that important seismic phases are captured in the Green's function and numerical noise is minimized.

After Green's functions for all receivers are obtained, they are substituted into Eq. (18) and a moment-tensor inversion can then be performed. Because the 1D model is an approximation of the real earth structure, errors such as differences in phase arrival times between the Green's functions and the observed seismograms exist. One way to reduce the effect of model error is to manually align *P*-wave arrival times

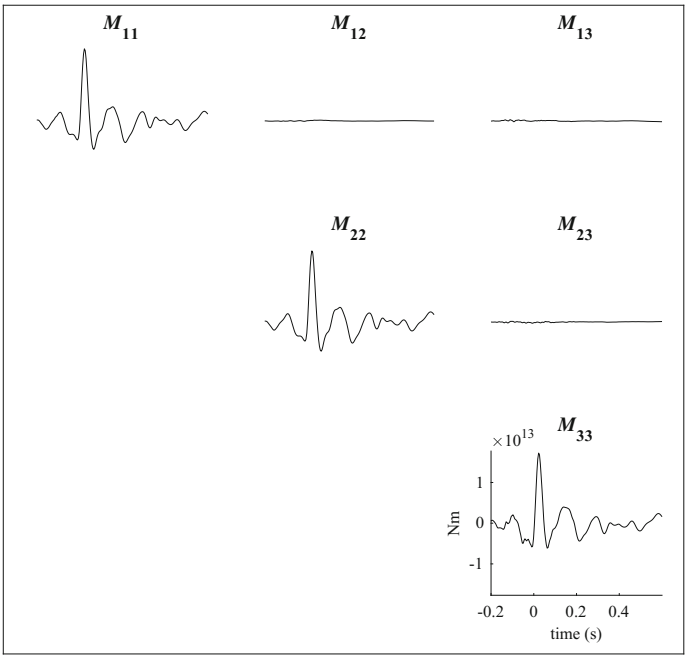

Fig. 5 Moment-tensor time histories of the explosion source from the inversion

between the Green's function and the observed signal before the Fourier transform. This procedure has been used in regional moment-tensor inversion studies (e.g., Zhao and Helmberger 1994), and it is a common practice in frequency-domain moment-tensor inversions. Even though the method does not correct for arrival-time error of later phases or amplitude errors, it still improves the inversion result. An additional measure that can be taken is to multiply the seismograms and the Green's functions by corresponding epicentral distances to some power. This is to increase amplitudes of seismograms at longer distances so that they provide similar contributions to the inversion result as close-in seismograms do. Multiplication by distance itself is a usual choice.

Figure 5 plots the moment tensor time histories of the explosion source from the inversion of seismograms shown in Fig. 4. Both manual alignment of *P*-wave arrival times and multiplication of seismograms by distance were applied before the inversion. The time histories provide detailed information about the source process including its mechanism, strength and evolution over time. It shows that the explosion-source moment tensor is dominated by its diagonal components. The source signal consists mainly of a single pulse that starts at time zero. All three diagonal components have similar wave shapes and amplitudes.

The isotropic nature of the source can be seen more clearly in its moment-rate spectra shown in Fig. 6. The amplitudes of the diagonal moment-rate spectra are

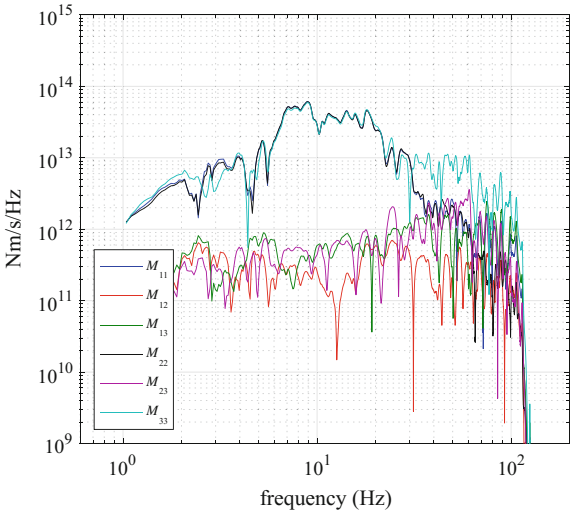

Fig. 6 The moment-rate spectra of the explosion source

almost identical between 5 and 25 Hz. Below 5 Hz, the diagonal-component spectra display an amplitude plateau possibly containing the static component, or the long-period level, of the source signal, which is used to estimate the source moment. When we integrate ground accelerations to ground velocities, we enhance the long-period noise in the data. As a result, we usually need to high-pass filter the seismograms. Because of the filtering, we see the roll-off of spectral amplitudes toward low frequencies. Below 20–30 Hz, off-diagonal-component spectral amplitudes are more than an order of magnitude lower than those of diagonal components. This is consistent with time-domain observations (Fig. 5).

Figure 7 plots the relative variance of the source moment-tensor spectra calculated using Eq. (20), assuming a unit data variance. The variance can be used to evaluate the reliability of the source spectra from the inversion. The variances of the diagonal moment-tensor components track each other closely for frequencies below 30 Hz. Above 30 Hz, the variance of M_{33} begins to increase significantly from those of M_{11} and M_{22}. We see corresponding deviation of M_{33} spectral amplitude in Fig. 6 for the same high frequencies. The correlation implies that the deviation could be caused by errors in modeling M_{33} at high frequencies and a physical interpretation of the deviation should be done with caution. Variances of off-diagonal components also increase with increasing frequency, meaning their spectra at high frequencies are not as well constrained either.

To further assess the quality of the inversion result, we usually compare observed seismograms used in the inversion with those predicted by the inversion result. Figure 8 shows such a comparison. Based on the correlation coefficient values, we conclude that the moment tensor from the inversion accurately reproduces observed signals particularly for vertical-component data and at closer distances.

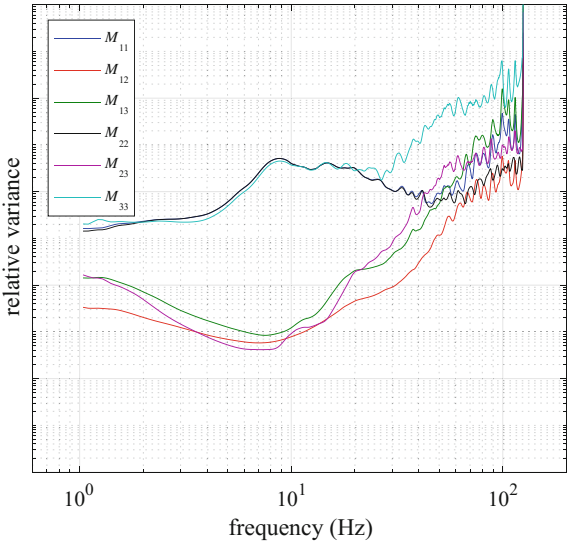

Fig. 7 Relative variance of moment-tensor spectra shown in Fig. 6

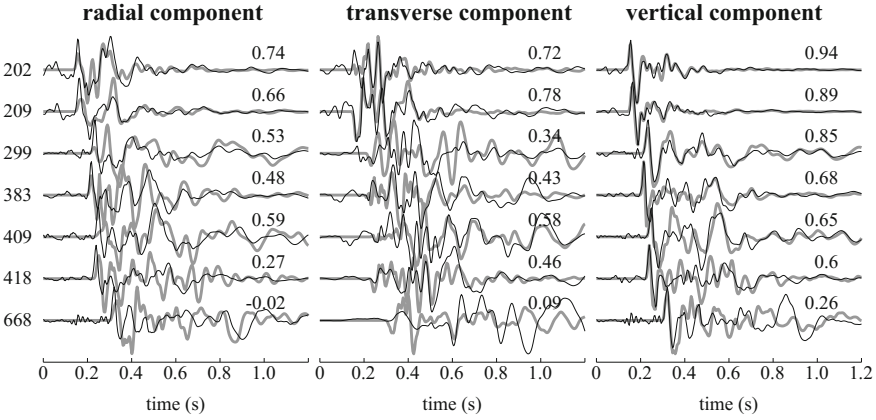

Fig. 8 A comparison between observed seismograms and synthetic seismograms predicted by the source moment tensor. Thick gray lines are observed seismograms. Trace amplitudes are normalized. Correlation coefficients between observed and predicted seismograms are marked above corresponding traces. Epicentral distances in meters are given on the far left of the figure

4.2 An Explosion-Induced Mine Collapse

In this example, we present the moment-tensor-inversion result of a mine collapse (Yang et al. 1998). The mine is an underground copper mine where the room-and-pillar method had been used to extract ore. The collapse was the intentional goal of an experiment where multiple pillars supporting a mined-out opening were explosively destroyed simultaneously. After the explosion-induced removal of pillars, the ceiling

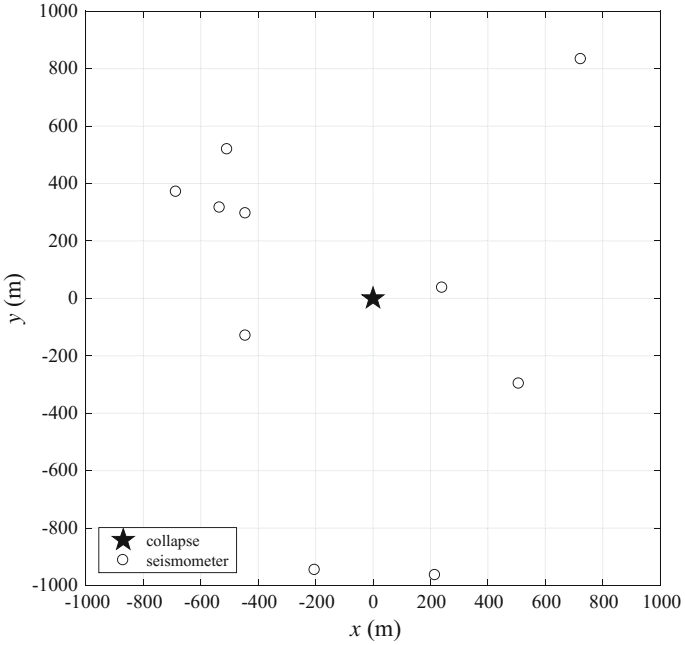

Fig. 9 Locations of the collapse and seismometers that recorded the collapse

collapsed upon the sudden loading of its own weight. The collapse occurred at a depth of 320 m below the earth's free surface and was recorded by seismometers deployed on the free surface. Figure 9 is a plan view of the locations of the collapse and seismometers that recorded the collapse. For this experiment, the seismometers have better azimuthal and distance coverage. The experiment design resulted in a better-constrained source moment tensor.

Figure 10 shows the mine-collapse moment-tensor time histories from the inversion. Again, the moment tensor is dominated by its diagonal components. This time, however, the three diagonal moment-tensor components do not have the same amplitudes. Among them, the vertical dipole M_{33} has the largest amplitude. This is consistent with the moment-tensor representation of a horizontal tension-crack model (Aki and Richards 2002).

Because we were able to retrieve the complete time history of the collapse source including its initiation and evolution, we gain better insight into the source process that would otherwise not be obtainable. One observation about this collapse from its moment-tensor time history is that the source started as an expansion source with positive onsets for all diagonal components. This is in contrast to accidental mine collapses that occur naturally as the result of the slow strain accumulation and final rock failure. Those collapses all start as implosional sources with dilatational seismic-wave first motions and negative onsets for their diagonal moment-tensor components (e.g., Taylor 1994; Pechmann et al. 1995). This unique collapse charac-

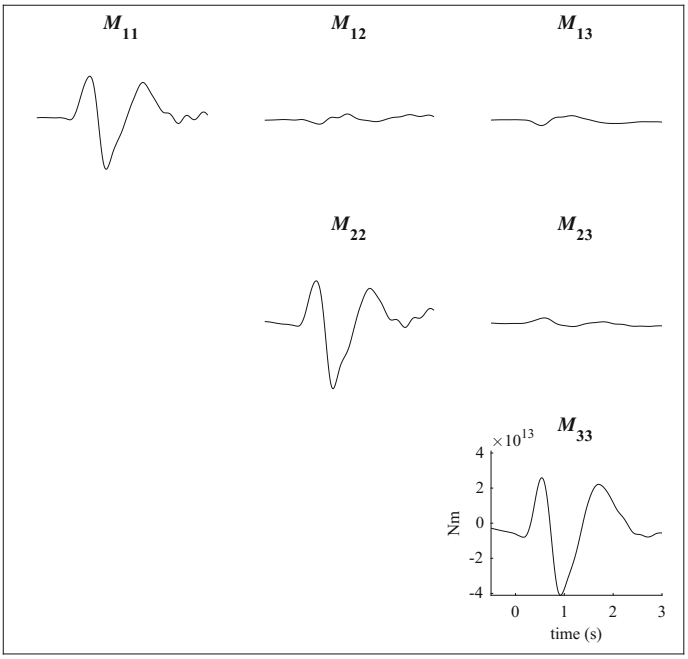

Fig. 10 Moment-tensor time histories of the explosion-induced mine collapse from the inversion

teristic motivated Yang et al. (1998) to propose a new model for the source process of this kind of explosion-induced mine collapses. This example illustrates the special power of the frequency-domain moment-tensor inversion technique.

4.3 Effects of Green's Functions on the Moment-Tensor Inversion

Because the process of moment-tensor inversion is essentially removing the propagation effects from observed seismograms to retrieve the source signal, it is apparent that accurate Green's functions that adequately represent the true path effects are critical to the success of the inversion. In this final example, we show how uncertainty in the velocity model used to calculate Green's functions can affect the resulting moment tensor.

This example is from another field experiment involving a small, contained underground chemical explosion. The explosion was recorded by seismometers within 700 m of the source. Refraction surveys were conducted around the test site during the experiment. As a result, the *P*-wave velocity structure was well constrained. The *S*-wave velocity, on the other hand, could not be determined reliably from available

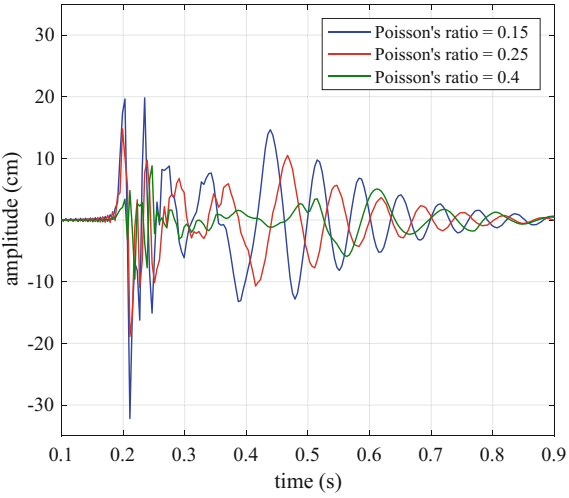

Fig. 11 Synthetic seismograms calculated using velocity models with different Poisson's ratios

data. As an alternative, *S*-wave velocities of the structure model were calculated based on *P*-wave velocities and different Poisson's ratios.

Figure 11 compares synthetic seismograms calculated using velocity models with different *S*-wave velocities corresponding to Poisson's ratios of 0.15, 0.25 and 0.4. Several observations can be made from the figure. As the Poisson's ratio increases, *S*-wave velocity decreases. This delays the arrival time of the surface wave (the long-period waves after about 0.35 s) significantly. In addition, the dominant frequency of the surface wave shifts to lower frequencies. Even though the quality factor Q of the velocity model remains the same, the amplitudes of the seismograms are reduced due to the decrease of the *S*-wave velocity. This is true not only for the surface-wave amplitude, but for the *P*-wave amplitude as well.

Figure 12 shows the effect of changing the *S*-wave velocity on the resulting moment tensor. We plot only results for Poisson's ratios of 0.15 and 0.4 as two end-member examples. For the Poisson's ratio of 0.15, the moment tensor has strong M_{13} and M_{23} signals. Among the diagonal components, M_{33} is much larger. As the Poisson's ratio increases to 0.4, the moment tensor looks much more like an isotropic-source moment tensor with dominant diagonal components that have similar amplitudes. The difference between the two moment tensors in terms of their source mechanisms is apparent, which poses a challenge to the reliable and quantitative interpretation of the source process.

Lessons learned from this example are that it is critically important to have an accurate velocity model for a moment-tensor inversion. Efforts should be made to constrain not only the *P*-wave velocity structure, but also *S*-wave-velocity and attenuation structures. In certain situations, a 3D model may be the only viable choice and Eq. (13), instead of Eq. (17), should be used.

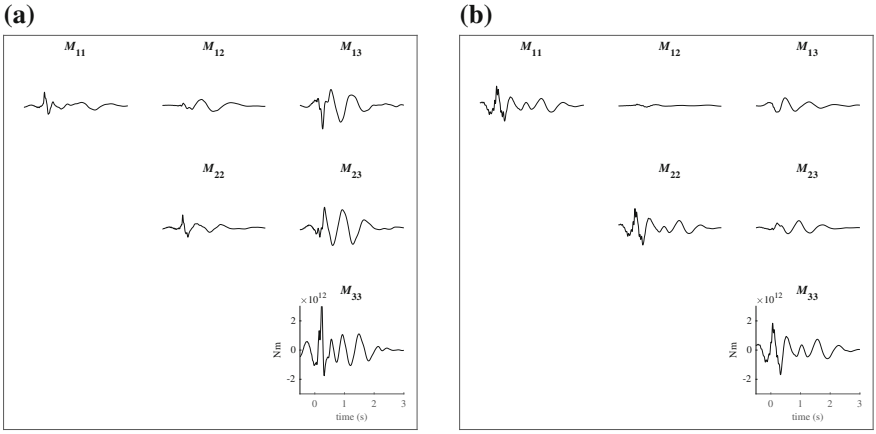

Fig. 12 Moment tensors from two inversions using Green's functions from two velocity models with Poisson's ratios of 0.15 (**a**) and 0.4 (**b**)

5 Conclusions

In this article, we described a frequency-domain moment-tensor inversion technique. Often used with near-source (e.g., <2 km) observations from small seismic sources, the method retrieves the complete source moment-tensor spectra and time histories, revealing detailed source information.

We provided examples illustrating the application and the advantage of the method. The last example highlights one of the issues that require attention in order to conduct successful frequency-domain moment-tensor inversions.

References

Aki K, Richards PG (2002) Quantitative Seismology, 2nd edn. University Science Books, Sausalito

Ekström G, Nettles M, Dziewoński AM (2012) The global CMT project 2004–2010: centroid-moment tensors for 13,017 earthquakes. Phys Earth Planet Int 200–201:1–9. https://doi.org/10.1016/j.pepi.2012.04.002

Julian BR, Miller AD, Foulger GR (1998) Non-double-couple earthquakes. 1. Theory. Rev Geophys 36(4):525

Leidig MR, Bonner JL, Reiter DT (2005) Development of a velocity model for Black Mesa, Arizona, and the southern Colorado Plateau from multiple data sets. Bull Seismol Soc Am 95(6):2136–2151

Menke W (1989) Geophysical data analysis: discrete inverse theory (rev edn). Academic Press, San Diego

Müller G (1985) The reflectivity method: a tutorial. J Geophys 58:153–174

Pechmann JC, Walter WR, Nava SJ et al (1995) The February 3, 1995, ML 5.1 seismic event in the trona mining district of southwestern Wyoming. Seism Res Lett 66(3):25–34

Pondrelli S, Salimbeni S, Morelli A et al (2011) European-Mediterranean regional centroid moment tensor catalog: solutions for 2005–2008. Phys Earth Planet Int 185(3–4):74–81. https://doi.org/10.1016/j.pepi.2011.01.007

Šílený J, Panza GF, Campus P (1992) Waveform inversion for point source moment tensor retrieval with variable hypocentral depth and structural model. Geophys J Int 109(2):259–274. https://doi.org/10.1111/j.1365-246X.1992.tb00097.x

Sipkin SA (1982) Estimation of earthquake source parameters by the inversion of waveform data: synthetic waveforms. Phys Earth Planet Int 30(2):242–259. https://doi.org/10.1016/0031-9201(82)90111-X

Stump BW, Johnson LR (1977) The determination of source properties by the linear inversion of seismograms. Bull Seismol Soc Am 67(6):1489–1502

Taylor SR (1994) False alarms and mine seismicity: an example from the Gentry mountain mining region, Utah. Bull Seismol Soc Am 84(2):350

Tsuruoka H, Kawakatsu H, Urabe T (2009) GRiD MT (grid-based real-time determination of moment tensors) monitoring the long-period seismic wavefield. Phys Earth Planet Int 175(1–2):8–16. https://doi.org/10.1016/j.pepi.2008.02.014

Yang X, Bonner JL (2009) Characteristics of chemical explosive sources from time-dependent moment tensors. Bull Seismol Soc Am 99(1):36–51. https://doi.org/10.1785/0120080243

Yang X, Stump BW, Phillips WS (1998) Source mechanism of an explosively induced mine collapse. Bull Seismol Soc Am 88(3):843–854

Zhao LS, Helmberger DV (1994) Source estimation from broad-band regional seismograms. Bull Seismol Soc Am 84(1):91–104